

Efficient pseudo-spectral solvers for the PKN model of hydrofracturing.

Michał Wrobel^(2,1), Gennady Mishuris^(1,2),

⁽¹⁾ *Institute of Mathematical and Physical Sciences, Aberystwyth University,
Ceredigion SY23 3BZ, Wales U.K.,*

⁽²⁾ *Eurotech Sp. z o.o.,
ul. Wojska Polskiego 3, 39-300 Mielec, Poland*

July 9, 2018

Abstract

In the paper, a novel algorithm employing pseudo-spectral approach is developed for the PKN model of hydrofracturing. The respective solvers compute both the solution and its temporal derivative. In comparison with conventional solvers, they demonstrate significant cost effectiveness in terms of balance between the accuracy of computations and densities of the temporal and spatial meshes. Various fluid flow regimes are considered.

1 Introduction and preliminary results

Hydraulic fracturing is a widely used method for stimulation of hydrocarbons reservoirs. This technology has been known and successfully applied for a few decades [14, 12, 6]. Recently it has been revived, due to economical reasons, as a basic technique for exploitation of unconventional deposits of oil and gas. The phenomenon of a fluid driven fracture propagating in a brittle medium is also present in many natural processes (e.g. magma driven dykes – [31], subglacial drainage of water – [34]).

Throughout the years, starting from the pioneering works of Sneddon and Elliot [32], Khristianovic and Zheltov [14], Perkins and Kern [30], Geertsma and de Klerk [11], and Nordgren [26], various models of hydrofracturing have been formulated and used in applications. A broad review of the topic can be found in [15, 16, 21, 17]. Together with increasing complexity of the models describing this multiphysics process, the computational techniques have been continuously enhanced. A comprehensive survey on the algorithms and numerical methods used in hydrofracturing simulation can be found in [4, 9].

Responding to the recent demand, an increasing stream of publications have appeared concerning additional information on seismic events, shear stresses in the rock formation, multifracturing and others and their implementation into the solvers [35, 25, 27, 8]. Also, a considerable effort has been made to improve the existing algorithms by incorporating new efficient numerical techniques [18, 21, 28, 29].

The main computational challenges associated with the modelling of hydraulic fractures are: a) strong nonlinearity resulting from the coupling between the solid and fluid phases, b) singularity of the gradients of the physical fields near the crack tip, c) moving boundaries, d) degeneration of the governing equations at the crack tip, multiscaling and others.

To achieve the maximal possible efficiency of numerical simulations, the computational algorithms should be formulated in *proper* variables accounting for all the problem peculiarities [21]. As a result, they allow one to reduce the volume of processed data, which is especially important when dealing with complex geometries and/or multifracturing.

The analysis presented in this paper is devoted to the PKN model of hydrofracturing. This model contains all the peculiarities mentioned above, except for the non-local relation for the fluid-solid coupling. Although we restrict our interest only to a single fracture, the developed algorithms, thanks to their robustness, can be successfully applied to model a system of cracks.

The numerical analysis of the problem should be backdated to Nordgren [26] who extended the Perkins and Kern model [30] to account for the fluid loss effect and fracture volume change. As a result, the crack length was determined as part of the solution. The author proposed a finite difference scheme to solve the problem, which is in fact equivalent to the finite volume (FV) method.

Further development of the PKN formulation was done by Kemp [13], who (a) implemented the specific boundary condition at the moving crack tip into the FV scheme, (b) incorporated asymptotic behaviour of the solution near the crack tip in a special tip element, (c) indirectly used the fourth power of the crack opening (w^4) as a new dependent variable, instead of the crack opening itself. For the early-time asymptotic model Kemp proposed a power series solution, presenting its first four terms.

The recent paper by Kovalyshen and Detournay[15] has extended most of Kemp's results, incorporating all information on the PKN model available to date. They present various asymptotics, complete analytical solution for an impermeable rock (directly extending the results from [13] from four leading terms to an infinite series representation), FV algorithm with a special tip element and a numerical benchmark for the Carter leak-off, linking the results to the scaling approach developed in [3, 7, 23, 24].

In [19]-[21], the PKN model was reformulated by Linkov to improve the efficiency and stability of computations by (i) introducing *proper* dependent variables (cubed fracture opening, w^3), (ii) utilizing the speed equation and (iii) by imposing a modified boundary condition at a small distance behind the crack tip (ε -regularisation). Additionally, the analytical solution for an impermeable rock was evaluated for the new dependent variable in a form of rapidly converging series in [21]. Moreover, the author highlighted in [19] that numerical schemes exploiting a fixed position of the crack tip during the iterations may become ill-posed.

In [22] and [17] the ε -regularisation technique was further enhanced by (i) appropriate adaptation of the speed equation to the chosen numerical scheme and (ii) improved way of imposing of the regularized boundary condition. A detailed discussion on various aspects of application of implicit and explicit numerical schemes was provided.

In this paper we are presenting a novel algorithm based on the pseudo-spectral approach. Namely, we propose an efficient numerical algorithm to solve a specific self-similar problem and extend the results to the general (transient) formulation. Since, the integration schemes used in the algorithm incorporate the exact boundary conditions at the crack tip, no regularization technique is necessary. The most accurate two points representation of the temporal derivative is used to guarantee an optimal algorithm performance. Finally, two solvers are developed which show their robustness and stability. They both demonstrate high cost effectiveness in terms of the relationship between the volume of the processed data and the accuracy of computations. Moreover, additionally to the crack opening and length, the temporal derivative of the former and the crack tip velocity are automatically returned as components of the problem solution.

1.1 Problem formulation

Let us consider a symmetrical crack of length $2l$ situated in the plane $x \in [-l, l]$. The crack is fully filled by a Newtonian liquid injected at the middle point ($x = 0$) with a known rate $q_0(t)$. Note here, that the crack length evolution, $l = l(t)$, is the result of fluid flow inside the fracture. Due to the symmetry of the problem, one can restrict the analysis to the half of the crack $x \in [0, l(t)]$.

The classic mathematical formulation of the PKN model of hydrofracturing was given in [26]. Below we present a system of equations constituting the model. The mass conservation principle is expressed

by the continuity equation:

$$\frac{\partial w}{\partial t} + \frac{\partial q}{\partial x} + q_l = 0, \quad t \geq t_0, \quad 0 \leq x \leq l(t), \quad (1)$$

while the Poiseuille equation describes the flow in a narrow channel. In the case of a Newtonian fluid, it is written in the following form:

$$q = -\frac{1}{M} w^3 \frac{\partial p}{\partial x}. \quad (2)$$

Here $w = w(t, x)$ stands for the crack opening, $q = q(t, x)$ is the fluid flow rate, $p = p(t, x)$ ($p = p_f - \sigma_0$, σ_0 - confining stress) refers to the net fluid pressure. The constant M , involved in the Poiseuille equation, is computed as $M = 12\mu$, where μ denotes the dynamic viscosity (see for example [1]). The function $q_l = q_l(t, x)$ from (1) is the volumetric rate of fluid loss to formation in the direction perpendicular to the crack surfaces per unit length of the fracture. This function is usually assumed to be given, but it may depend on the solution itself as well. To account for various leak-off regimes, we accept the following behaviour of q_l :

$$q_l(t, x) = Q_l(t)(l(t) - x)^\eta, \quad \text{for } x \rightarrow l(t), \quad (3)$$

for some constant $\eta \geq -1/2$. Note that the case $\eta = -1/2$ corresponds to the Carter law [5], while $\eta \geq 1/3$ guarantees that the leak-off vanishes near the crack tip as fast as the crack opening at least (see for details [17]).

The group of fluid equations is to be supplemented by the relation describing deformation of the rock under applied hydraulic pressure. In the case of the PKN model, a linear relationship between the net fluid pressure and crack opening is in use:

$$p = kw, \quad (4)$$

where a known proportionality coefficient $k = \frac{2}{\pi h} \frac{E}{1-\nu^2}$ is found from the solution of a plane strain elasticity problem [26] for an elliptical crack of height h . E and ν are the elasticity modulus and Poisson's ratio, respectively.

The above equations are equipped with the boundary condition at a crack mouth ($x = 0$) determining the injection flux rate:

$$-\frac{k}{M} \left[w^3 \frac{\partial w}{\partial x} \right]_{x=0} = q_0(t), \quad (5)$$

and two boundary conditions at a crack tip:

$$w(t, l(t)) = 0, \quad q(t, l(t)) = 0. \quad (6)$$

In order to define the crack length, $l(t)$, the global fluid balance equation is usually utilized (see for example [4])

$$\begin{aligned} \int_0^{l(t)} [w(t, x) - w(0, x)] dx - \int_0^t q_0(t) dt + \\ \int_0^{l(t)} \int_0^t q_l(t, x) dt dx = 0. \end{aligned} \quad (7)$$

Finally, the initial conditions are assumed in the following way:

$$w(0, x) = 0, \quad l(0) = 0. \quad (8)$$

System (1) – (8) constitutes the classic formulation of the PKN problem. It was shown in [13] and [10] that the asymptotic behaviours of w and q near the crack tip are interrelated, and the first term of the expansion for the crack opening may be written as:

$$w(t, x) \sim w_0(t) (l(t) - x)^\alpha, \quad \text{as } x \rightarrow l(t). \quad (9)$$

For the classic PKN model the exponent $\alpha = 1/3$ was found in [13]. Thus condition $(6)_2$ is always satisfied as it follows from (2) and (4). As a result, the model does not account for the standard stress singularity of fracture mechanics at the crack tip, and thus is relevant for the so-called zero toughness regime (see e.g. [1]).

REMARK 1. Despite that zero crack opening and length are considered as the initial conditions, all authors begin their studies from the asymptotic model for the small time. With the assumption of zero leak-off term in the continuity equation and constant q_0 , the problem is reduced to a self-similar formulation. The full numerical analysis is then continued by taking the similarity solution as the initial state. This effectively means that the initial conditions (8) can be replaced by the non-zero crack opening

$$l(0) = l_\diamond, \quad w(0, x) = w_\diamond(x), \quad x \in (0, l_\diamond). \quad (10)$$

In this paper, the modified formulation of the PKN model is considered, following the recent advance in the area of numerical modelling [19, 20, 21, 22]. Thus, to trace the fracture front we use the so-called speed equation, instead of the fluid balance relationship (7):

$$\frac{dl}{dt} = v_0(t) = \frac{q}{w} \Big|_{x=l(t)}. \quad (11)$$

The speed equation assumes that the fracture tip coincides with the fluid front, which excludes the presence of a lag or an invasive zone ahead of the fracture tip. Originally it was introduced by Kemp [13] and has been recently revisited by Linkov [19, 20, 21].

Note that, on substitution of equations (2), (4) and (9) into (11), one obtains a relationship between the crack propagation speed and the multiplier of the leading term of the crack opening asymptotic expansion (9):

$$\frac{dl}{dt} = \frac{k}{3M} w_0^3(t). \quad (12)$$

This implies that the quality of the numerical estimation of w_0 (see estimate (9)) should be vital for the accuracy of computations.

By substituting the Poiseuille equation (2) into the continuity equation (1) one obtains a lubrication (Reynolds) equation for the considered problem, where the net fluid pressure function $p(t, x)$ is eliminated:

$$\frac{\partial w}{\partial t} - \frac{k}{M} \frac{\partial}{\partial x} \left(w^3 \frac{\partial w}{\partial x} \right) + q_l = 0, \quad t \geq t_0, \quad 0 \leq x \leq l(t). \quad (13)$$

In this way the modified formulation of the PKN model includes: i) the Reynolds equation (13); ii) the boundary conditions (5) – (6)₁; iii) the asymptotics (9); iv) the initial conditions (10); v) the speed equation in the form (12).

The paper is organized as follows: in the next subsection we present the normalized formulation of the problem. Then, two types of self-similar solutions for the PKN model are discussed. These solutions are used in section 2 to investigate a numerical algorithm for a time independent variant of the problem. In section 3, the algorithm is modified to tackle the transient regime. Two alternative integral solvers are developed and their performances and applicability are examined. Section 4 contains the final conclusions.

1.2 Normalized formulation.

Following [17], we normalize the problem by introducing dimensionless variables:

$$\tilde{x} = \frac{x}{l(t)}, \quad \tilde{t} = \frac{t}{t_n}, \quad t_n = \frac{M}{kl_\diamond}, \quad \tilde{w}_\diamond(\tilde{x}) = w_\diamond(x),$$

$$\tilde{w}(\tilde{t}, \tilde{x}) = \frac{w(t, x)}{l_\diamond}, \quad L(\tilde{t}) = \frac{l(t)}{l_\diamond}, \quad l_\diamond^2 \tilde{q}_0(\tilde{t}) = t_n q_0(t), \quad (14)$$

$$\tilde{l}_\diamond \tilde{q}_l(\tilde{t}, \tilde{x}) = t_n q_l(t, x), \quad l_\diamond^{2/3} \tilde{w}_0(\tilde{t}) / L^{1/3}(\tilde{t}) = w_0(t),$$

where $\tilde{x} \in [0, 1]$, $L(0) = 1$.

In the new variables equation (13) reads:

$$\frac{\partial \tilde{w}}{\partial \tilde{t}} - \tilde{x} \frac{L'}{L} \frac{\partial \tilde{w}}{\partial \tilde{x}} - \frac{1}{L^2(\tilde{t})} \frac{\partial}{\partial \tilde{x}} \left(\tilde{w}^3 \frac{\partial \tilde{w}}{\partial \tilde{x}} \right) + \tilde{q}_l = 0, \quad (15)$$

$$\tilde{t} \geq 0, \quad 0 \leq \tilde{x} \leq 1.$$

The boundary conditions (5) – (6)₁ may be rewritten as:

$$-\frac{1}{L(\tilde{t})} \left[\tilde{w}^3 \frac{\partial \tilde{w}}{\partial \tilde{x}} \right]_{\tilde{x}=0} = \tilde{q}_0(\tilde{t}), \quad \tilde{w}(\tilde{t}, 1) = 0. \quad (16)$$

The initial conditions (10) are defined as:

$$L(0) = 1, \quad \tilde{w}(0, \tilde{x}) = \tilde{w}_0(\tilde{x}), \quad \tilde{x} \in [0, 1]. \quad (17)$$

The asymptotic expansion for crack opening (9) takes the form:

$$\tilde{w}(\tilde{t}, \tilde{x}) \sim \tilde{w}_0(\tilde{t})(1 - \tilde{x})^{1/3}, \quad \text{for } \tilde{x} \rightarrow 1. \quad (18)$$

For the sake of completeness of the normalization, we also present the global fluid balance equation (7), although it will not be used later on:

$$\begin{aligned} L(\tilde{t}) \int_0^1 \tilde{w}(\tilde{t}, x) dx - \int_0^1 \tilde{w}(0, x) dx - \int_0^{\tilde{t}} \tilde{q}_0(t) dt \\ + \int_0^{\tilde{t}} L(t) \int_0^1 \tilde{q}_l(t, x) dx dt = 0. \end{aligned} \quad (19)$$

Finally, the transformation of the speed equation (12) yields:

$$\frac{d}{dt} L(\tilde{t}) = V_0(\tilde{t}) = \frac{1}{3L(\tilde{t})} \tilde{w}_0^3(\tilde{t}). \quad (20)$$

As shown in [22], equation (20) is convenient to trace the fracture front when standard ODE solvers are in use for the dynamic system describing the problem. On the other hand, the crack length can be computed from (20) by direct integration to give:

$$L(\tilde{t}) = \sqrt{1 + \frac{2}{3} \int_0^{\tilde{t}} \tilde{w}_0^3(\tau) d\tau}, \quad (21)$$

which is useful when an implicit method (for example Crank-Nicolson scheme) is utilised (see [22]).

On substitution of (20) into (15) one can rewrite the later to obtain:

$$3L^2 \left(\frac{\partial \tilde{w}}{\partial \tilde{t}} + \tilde{q}_l(\tilde{t}, \tilde{x}) \right) = \tilde{x} \tilde{w}_0^3 \frac{\partial \tilde{w}}{\partial \tilde{x}} + 3 \frac{\partial}{\partial \tilde{x}} \left(\tilde{w}^3 \frac{\partial \tilde{w}}{\partial \tilde{x}} \right). \quad (22)$$

In the following, equation (22) will be used as a basic relation to formulate our integral solvers.

From now on, for convenience, we shall omit the tilde symbol in all quantities. In this way all the notations refer henceforth to the normalized formulation.

1.3 Self-similar solutions

Let us assume

$$q_l(t, x) = \gamma e^{\gamma t} q_l^*(x), \quad (23)$$

and look for the similarity solution of the problem in the form:

$$w(t, x) = u(x)e^{\gamma t}, \quad w_0(t) = u_0 e^{\gamma t}, \quad (24)$$

where the asymptotic behaviour (18) holds true, and u_0 is the limiting value of u defined in the same manner as in estimate (18). Thus, equation (20) transforms to an identity if one takes:

$$L^2(t) = \frac{2u_0^3}{9\gamma} e^{3\gamma t}. \quad (25)$$

On substitution of (23), (24), and (25) into the equation (22) one can reduce the latter to the following ordinary differential equation:

$$\beta u_0^3 (u + q_l^*) = \mathcal{A}(u), \quad (26)$$

with $\beta = 2/3$. Here, the nonlinear differential operator \mathcal{A} is defined by the right-hand side of equation (22) and is equipped with the boundary conditions

$$-3u_0^{-3/2} \left[u^3 \frac{du}{d\tilde{x}} \right]_{\tilde{x}=0} = q_0^*, \quad u(1) = 0, \quad (27)$$

where we have introduced an auxiliary notation:

$$q_0^* = \sqrt{\frac{2}{\gamma}} e^{-\frac{5\gamma t}{2}} q_0(t). \quad (28)$$

If q_0^* is constant, then equation (26) together with the boundary conditions (27) do not depend on time and constitute a boundary value problem (BVP) degenerated at point $x = 1$. Indeed, the nonlinear coefficient in front of the second order term of the differential operator vanishes at the point $x = 1$ in view of the boundary condition (27)₂. This BVP is in fact a self-similar formulation of the original problem with specific, given leak-off regime and the inlet flux.

Other class of similarity solutions can be found, for some $a \geq 0$, by assuming:

$$q_l(t, x) = \gamma(t + a)^{\gamma-1} q_l^*(x), \quad w(t, x) = (t + a)^\gamma u(x), \quad (29)$$

$$L^2(t) = \frac{2u_0^3}{3(3\gamma + 1)} (a + t)^{3\gamma+1}. \quad (30)$$

As a result, one again obtains the BVP (26) – (27) with $\beta = 2\gamma/(3\gamma + 1)$ and

$$q_0^* = \sqrt{\frac{6}{(3\gamma + 1)}} (a + t)^{\frac{1-5\gamma}{2}} q_0(t). \quad (31)$$

Thus, for $\gamma = 1/5$ the self-similar solution corresponds to the constant injection flux rate, while the crack propagation speed decreases with time as $L'(t) = O(t^{-1/5})$ for $t \rightarrow \infty$. If, however, one takes $\gamma = 1/3$, the crack propagation speed is constant and the injection flux rate increases with time: $q_0(t) = O(t^{1/3})$ for $t \rightarrow \infty$.

Note that self-similar solutions do not necessarily satisfy the initial conditions (17) as the normalised initial crack lengths are:

$$L(0) = \sqrt{\frac{2u_0^3}{9\gamma}}, \quad L(0) = \sqrt{\frac{2u_0^3 a^{3\gamma+1}}{3(3\gamma+1)}},$$

for the first and the second type, respectively.

REMARK 2. As one can see the second type of similarity solution has a physical sense for any $-1/3 < \gamma < \infty$ and thus, can be used to model three different transient regimes of the crack evolution: crack acceleration ($\gamma > 1/3$), crack deceleration ($\gamma < 1/3$), and a steady-state propagation of the fracture ($\gamma = 1/3$). The first type of solution possesses a physical interpretation only for positive values of γ , which restricts its application to the cases of accelerating crack.

The self-similar solutions formulated above are used in the following sections to analyse computational accuracy provided by the developed solvers. So far to this end, the asymptotic models have been usually employed [26, 13, 15, 21]. However, all of them are restricted to the case of a constant influx, q_0 .

2 Numerical solution of the self-similar problem

In this section we will formulate an algorithm of the solution for the self-similar problem defined by equation (26) and the boundary conditions (27). The following representation of the sought function $u(x)$ will be accepted:

$$u(x) = u_0(1-x)^{1/3} + \Delta u(x). \quad (32)$$

It results from the asymptotic behaviour (18) and $\Delta u(x) = O((1-x)^\zeta)$ for $x \rightarrow 0$. Parameter $\zeta > 1/3$ depends strongly on the behavior of the leak-off function q_l near the crack tip. In particular, when q_l vanishes near the crack tip in the same manner as the solution, or faster, ($\eta \geq 1/3$) then $\zeta = 4/3$. One can show that (compare (3))

$$\zeta = \min\{4/3, 1 + \eta\} \geq 1/2, \quad (33)$$

see also [17] for details.

2.1 Integral solver for the self-similar problem.

Below we present an algorithm to solve equation (26) by numerical inversion of the operator \mathcal{A} . Exploiting the solution representation (32), the inverse operator \mathcal{A}^{-1} defines both components: u_0 and Δu . To derive \mathcal{A}^{-1} , we integrate the equation (26) twice over the interval $[x, 1]$ taking into account the boundary condition (27)₂. Then, after simple transformations one obtains:

$$\begin{aligned} 3u_0^3(1-x)\Delta u &= -\frac{3}{4}[6u_0^2(1-x)^{2/3}(\Delta u)^2 + \\ &4u_0(1-x)^{1/3}(\Delta u)^3 + (\Delta u)^4] + u_0^3 \int_x^1 \Delta u d\xi + \\ &2u_0^3 \int_x^1 (\xi-x)u d\xi - (1-x)u_0^3 \int_x^1 u d\xi + \\ &\beta u_0^3 \int_x^1 (\xi-x)(u + q_l^*) d\xi. \end{aligned} \quad (34)$$

In short, the latter can be symbolically written in the compact form:

$$\Delta u = G_1(\beta, u_0, \Delta u) + G_2(\beta, u_0, \Delta u, q_l^*), \quad (35)$$

where the operators involved in the right-hand side are defined as follows:

$$\begin{aligned} 3u_0^3(1-x)G_1 = & -\frac{3}{4}[6(u_0^2(1-x)^{2/3}(\Delta u)^2 + \\ & 4u_0(1-x)^{1/3}(\Delta u)^3 + (\Delta u)^4] + \\ & (2+\beta)u_0^3 \int_x^1 (\xi-x)\Delta u d\xi, \end{aligned} \quad (36)$$

$$\begin{aligned} 3(1-x)G_2 = & x \int_x^1 \Delta u d\xi + \frac{3}{28}(3\beta-1)u_0(1-x)^{7/3} + \\ & \beta \int_x^1 (\xi-x)q_l^* d\xi. \end{aligned} \quad (37)$$

One can conclude from (3) and (18) that for $x \rightarrow 1$

$$G_1 = O((1-x)^{1+\zeta}), G_2 = O((1-x)^\zeta), \quad (38)$$

where ζ defined in (33).

The relation to compute u_0 is derived by integration of (26) with respect to x from 0 to 1. Then, taking into account the representation (32) and the boundary condition (27)₁, one can formulate the condition:

$$G_3(\beta, u_0, \Delta u, q_0^*) = 0, \quad (39)$$

where

$$\begin{aligned} G_3 = & \frac{3}{4}(\beta+1)u_0^{5/2} + \\ & u_0^{3/2} \left[(\beta+1) \int_0^1 \Delta u dx + \beta \int_0^1 q_l^* dx \right] - q_0^*. \end{aligned}$$

It is easy to prove that for any $q_0^* > 0$ and $\beta > -1$ there exists a unique positive solution u_0 of equation (39), regardless of the values of the functions Δu and q_l^* .

The inverse operator \mathcal{A}^{-1} is defined, by equations (35) and (39), as:

$$[u_0, \Delta u] = \mathcal{A}^{-1}(\beta, q_l^*, q_0^*). \quad (40)$$

Its numerical execution is based on the following iterative algorithm:

$$\begin{cases} G_3(\beta, u_0^{(i+1)}, \Delta u^{(i)}, q_0^*) = 0, \\ \Delta u^{(i+1)} = G_1(\beta, u_0^{(i+1)}, \Delta u^{(i)}) + \\ \quad G_2(\beta, u_0^{(i+1)}, \Delta u^{(i)}, q_l^*), \end{cases} \quad (41)$$

where superscripts refer to the consequent iterations. In the first step we assume that:

$$\Delta u^{(0)} = 0. \quad (42)$$

Of course, if any better approximation is available, it can replace (42). Note the first relation of (41) is a nonlinear algebraic equation that can be solved e.g. by the Newton-Raphson method, while the second equation is a typical iterative relationship.

2.2 Numerical examples and discussions

In this section we investigate the performance of the numerical algorithm (41) – (42). To this end, the power law type self-similar solution (29) is utilized as a benchmark. Apart from the fact that the equations for other self-similar solution (24) look identically, the value of the parameter β appearing in the exponential benchmark is always the same ($\beta = 2/3$). Thus the power law type self-similar benchmark gives us an opportunity to manipulate with the value of β , which will be crucial for further implementation of the algorithm to the transient regime.

Let us utilize the following variant of benchmark solution used previously in [22] (compare (63) in the Appendix A):

$$\begin{aligned} u(x) &= (1-x)^{1/3}(1+s(x)), \\ s(x) &= -\frac{1}{8e} \left(\frac{1}{3} - \frac{2\gamma}{3\gamma+1} \right) (1-x) + 0.05(1-x)^2, \end{aligned} \quad (43)$$

which yields $\eta = 4/3$.

Computations are carried out for different meshes based on $N + 1$ nodal points:

$$x_j^{(\varrho)} = 1 - \left(1 - \frac{j}{N}\right)^\varrho, \quad j = 0, 1, \dots, N. \quad (44)$$

When one sets $\varrho = 1$, the points of spatial mesh are uniformly distributed over the whole interval - this mesh will be called the *uniform mesh*. By taking $\varrho > 1$ we obtain increased mesh density while approaching the end point $x = 1$ (the larger ϱ the greater mesh density near the crack tip) - this mesh will be referred to as the *non-uniform mesh*. In our computations we will use $\varrho = 3$. This choice is motivated by the following reason. To increase the solution accuracy, we compute integral operators from (41) using the classic Simpson quadrature, which gives an error controlled by the fourth derivative of the integrand. Accounting for the asymptotic behaviour of the solution, the transformation (44), for $\varrho = 3$, improves the smoothness of the integrand with respect to the new independent variable near the crack tip (replaces the fraction powers function). In this way, the error of integration can be minimized. We shall confirm this below in numerical tests.

We use two parameters as the measures of computational accuracy: (i) – the maximal point-wise relative error (denoted as: δu) of the complete solution $u(x)$ and (ii) – a relative error (denoted by δu_0) of the coefficient u_0 defining the leading asymptotic term in (32).

The efficiency of computations will be assessed by the number of iterations needed to compute the solution. The iterative process is stopped in each case when the L_2 -norm of the relative difference between two consecutive approximations becomes smaller than $\epsilon = 10^{-10}$. Finally, we analyze how the solution errors depend on the number of nodal points N .

The computations revealed that convergence of the iterative process (41) may only be achieved for some range of β values. For the analyzed benchmark it was: $\beta \in [-1.8, 4.8]$. In fact, this interval is wider than one could expect and fully covers any physically motivated values of $\beta \in (0, 2/3)$ following from the self-similar formulation. Interestingly, there are also solutions for $\beta < -1$ (compare discussions after equation (39)). This information shall be used later on, to construct a solver for transient regimes.

In Fig. 1a) the values of δu and δu_0 obtained for the analyzed benchmark (43) are shown. The computations were done for the meshes composed of 100 nodes. As can be seen, the non-uniform mesh gives at least one order better accuracy of the solution, for the same number of nodal points. The error of u_0 is lower than the error of the complete solution $u(x)$, as one could expect, while its distribution is not as smooth as for $\delta u(x)$. The minimum of $\delta u(x)$ is located near $\beta = 1/3$ which corresponds to the steady-state similarity solution. Interestingly, in the case of the uniform mesh the aforementioned minimum is deeper and sharper than for the non-uniform one.

Fig. 1b) depicts the number of iterations needed to obtain the final solution for different values of β . It shows that the convergence rate almost does not depend on the type of mesh chosen. The best

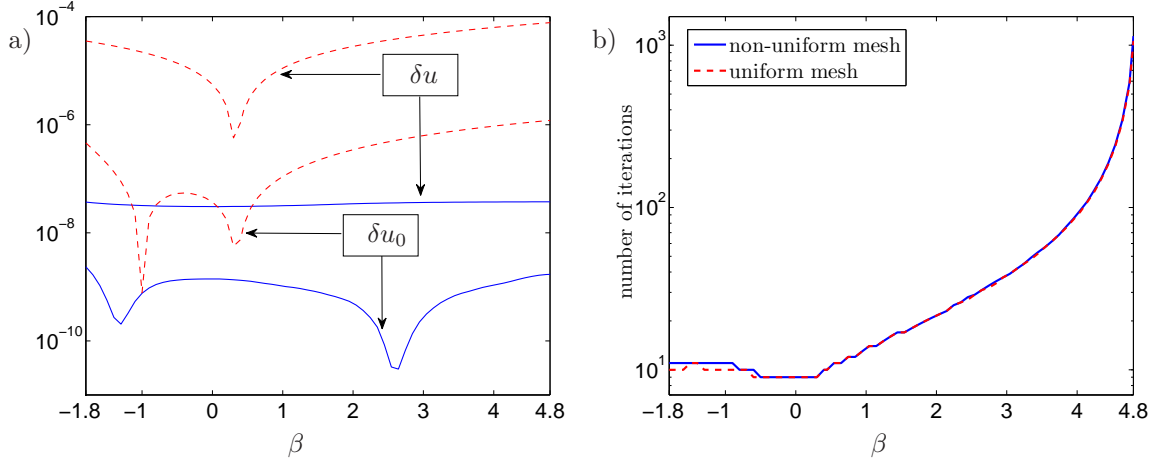


Figure 1: a) The accuracy of computations: maximal relative error of $u(x)$ and u_0 as a function of β ; b) Number of iterations to reach the final solution as a function of β . Dashed lines refer to the uniform mesh, solid lines to the non-uniform mesh (for $\varrho = 3$).

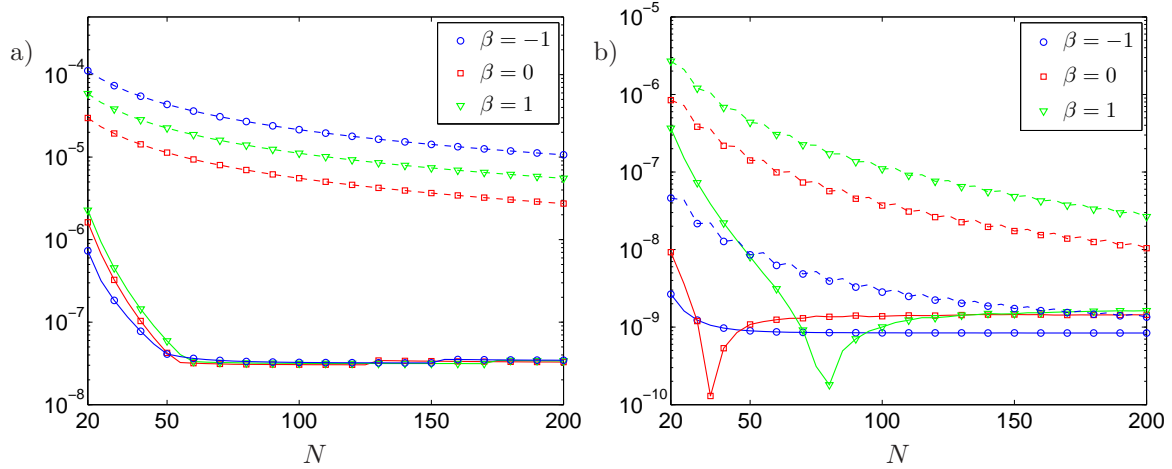


Figure 2: The maximal relative error of solution as a function of the number of nodal points N : a) δu , b) δu_0 . Dashed lines refer to the uniform mesh, solid lines to the non-uniform mesh (for $\varrho = 3$).

efficiency of computations appears for approximately $|\beta| < 1/2$. Note that this interval corresponds to the values of β which provide the best accuracy of computations. The time of computations (number of iterations) increases with $|\beta|$ growth, however this trend does not exhibit a bilateral symmetry (for negative and positive values of β). Moreover, the cost of computations increases with the solution error.

Fig. 2 shows how the accuracy of computations depends on the number of nodal points N . Both chosen meshes are analyzed for three different values of $\beta = -1, 0, 1$. It can be seen that the non-uniform mesh gives at least two orders of magnitude better accuracy than the regular one. For both types of meshes, the values of δu_0 are much lower than respective δu , however the best result for δu_0 does not necessarily correspond to the best δu (e.g. $\beta = -1$ for the regular mesh). The non-uniform mesh

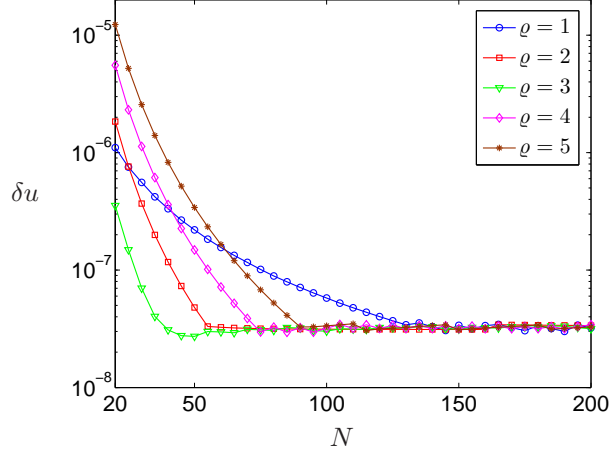


Figure 3: The maximal relative error of solution δu_0 for various spatial meshes. Computations were done for $\beta = 1/3$.

provides much lower sensitivity of solution accuracy to the variation of β than the uniform one. Also the maximal level of accuracy is obtained much faster for the non-uniform mesh. In the considered case, it is sufficient to take only 60 nodal points to achieve the maximal possible accuracy.

The last test in this subsection identifies the influence of spatial meshing on the solution accuracy. To this end, we consider the following values of $\varrho = 1, 2, \dots, 5$ from representation (44). The benchmark taken here accepts $\beta = 1/3$, as it provides the best accuracy and will be important in next subsections. For each of the values of ϱ , a characteristic $\delta u(N)$ was computed. The results are presented in Fig. 3. It shows that, regardless of the mesh under consideration (or equivalently, the value of the parameter ϱ), the maximal achievable accuracy is the same. However, this ultimate level is reached for different numbers of nodal points, N . The fastest convergence takes place for $\varrho = 3$, which confirms our previous predictions on the optimal choice of the spatial meshing. The slowest convergence to the saturation level manifests the uniform mesh ($\varrho = 1$).

The overall influence of the value of the parameter ϱ on the accuracy of computations results from the following trend: the larger the value of ϱ the lower error near the crack tip and the greater error near the crack inlet. The optimal balance between the local errors is observed for $\varrho = 3$, which confirms our predictions. In the following, only the non-uniform mesh for $\varrho = 3$ will be used in computations.

3 Solution to the transient problem

In this section we adopt the idea of the integral solver, developed for the self-similar formulation, to the transient regime. The basic assumptions of the approach remain the same, however the algorithm has to be modified in some essential aspects. First of all, one has to build the mechanism of temporal derivative approximation into the numerical procedure together with necessary measures to stabilize the algorithm. We will propose two methods of doing this, constructing in fact two different solvers. The second fundamental difference between the self-similar and time-dependent formulations is that in the latter case, the crack length $L(t)$ becomes now an element of the solution, which should be looked for simultaneously with the crack opening $w(t, x)$ and the first term of its asymptotics near the crack tip $w_0(t)$.

The basic system of equations for the transient problem is composed of: the governing equation (22),

the boundary conditions (16), the initial conditions (17) and the integral equation defining the crack length (21).

To avoid using multiple subscripts let us adopt the following manner of notation:

$$w(t_j, x) = w(x), \quad w(t_{j+1}, x) = W(x). \quad (45)$$

Consequently, the asymptotic representations of the solution near the crack tip read:

$$\begin{aligned} w(x) &= w_0(1-x)^{1/3} + \Delta w, \\ W(x) &= W_0(1-x)^{1/3} + \Delta W, \end{aligned} \quad x \rightarrow 1, \quad (46)$$

where ζ is defined in (33) and

$$\Delta w = O((1-x)^\zeta), \quad \Delta W = O((1-x)^\zeta), \quad \text{as } x \rightarrow 1.$$

3.1 Solver using self-similar algorithm (40) – (41)

Below, we show the way to convert the initial boundary value problem defined by equations (16), (21), (22) to the form which may be tackled by the integral solver in the form (41) for the self-similar solution. Obviously, system (41) is to be supplemented with an additional equation defining the crack length.

The main idea of the approach is to use the temporal derivative as one of the dependent variables in the numerical procedure. To achieve this, we compute the derivative of the solution at each time step $t = t_{j+1}$ in the following iterative process:

$$\begin{aligned} \frac{\partial W^{(i+1)}}{\partial t} &= G_4\left(\sigma^{(i+1)}, W^{(i+1)}, \frac{\partial W^{(i)}}{\partial t}\right) \equiv \\ &\sigma^{(i+1)} \frac{W^{(i+1)} - w}{\Delta t} + \left(1 - \sigma^{(i+1)}\right) \frac{\partial W^{(i)}}{\partial t}, \end{aligned} \quad (47)$$

where superscripts refer to the number of iteration, $\Delta t = t_{j+1} - t_j$ and the values of $\sigma^{(i+1)}$ are to be defined later. The first approximation of the temporal derivative is

$$\frac{\partial W^{(1)}}{\partial t} = \frac{\partial w}{\partial t}. \quad (48)$$

Note that the derivative at initial time $t = 0$ can be immediately found from the governing equation (22) by substitution of the initial conditions.

Substituting (47) into (22) one obtains the problem (26) and (27) with respect to the unknown function $W(x)$ by exploiting the following convention:

$$\begin{aligned} q_l^* &= -w + \frac{\Delta t}{\sigma^{(i+1)}} \left[(1 - \sigma^{(i+1)}) \frac{\partial W^{(i)}}{\partial t} + q_l(t, x) \right], \\ \beta W_0^3 &= \frac{3\sigma^{(i+1)}}{\Delta t} \left(L^{(i+1)} \right)^2, \end{aligned} \quad (49)$$

and

$$q_0^*(t) = 3q_0(t)W_0^{-3/2}L^{(i)}. \quad (50)$$

Finally, the crack length from equation (21) can be iterated as:

$$L^{(i+1)} = G_5(W_0) \equiv \sqrt{(L^{(i)})^2 + \frac{\Delta t}{3}(W_0^3 + w_0^3)}. \quad (51)$$

Here the integral from (21) is computed by the trapezoidal rule, taking into account the information obtained from the previous time steps ($t \leq t_j$).

In this way the governing partial differential equation and all the boundary conditions have been transformed to the formulation used previously in the self-similar problem. As a result, respective integral operators (34) – (37) and (39) remain the same with modified arguments (49) and (50), where (51) should be taken into account.

To choose the value of the parameter $\sigma^{(i+1)}$ at each iterative step, let us recall that the best performance of the algorithm described in subsection 2.2 has been achieved near $\beta = 1/3$. Taking this fact into account in (49)₂, one can choose

$$\sigma^{(i+1)} = \frac{\Delta t \left(W_0^{(i+1)} \right)^3}{9 \left(L^{(i+1)} \right)^2}. \quad (52)$$

Thus, the inverse operator for \mathcal{A} , defining the solution of the transient problem at the time step $t = t_{j+1}$, can be expressed in the following manner (compare (40)):

$$\left[W_0, L, \Delta W, \frac{\partial W}{\partial t} \right] = \hat{\mathcal{A}}^{-1}(1/3, q_l^*, q_0^*). \quad (53)$$

The iterative algorithm of the solver can be described by the system:

$$\begin{cases} G_3 \left(1/3, W_0^{(i+1)}, \Delta W^{(i)}, q_0^* \right) = 0, \\ \Delta W^{(i+1)} = G_1 \left(1/3, W_0^{(i+1)}, \Delta W^{(i)} \right) + \\ \quad G_2 \left(1/3, W_0^{(i+1)}, \Delta W^{(i)}, q_l^* \right), \\ L^{(i+1)} = G_5 \left(W_0^{(i+1)} \right), \\ \frac{\partial W^{(i+1)}}{\partial t} = G_4 \left(\sigma^{(i+1)}, W^{(i+1)}, \frac{\partial W^{(i)}}{\partial t} \right), \end{cases} \quad (54)$$

Note that parameters $q_0^* = q_0^{*(i)}$, $q_l^* = q_l^{*(i+1)}$ and $\sigma^{(i+1)}$ are also iterated according to (49)₁, (50) and (52). To finalize the algorithm, it is enough to define the initial forms of the crack opening $W^{(1)}$ and the crack length $L^{(1)}$. This is achieved by choosing

$$W^{(1)} = w + \frac{\partial w}{\partial t} \Delta t, \quad L^{(1)} = L(t_i), \quad (55)$$

which finishes the description of the computation scheme for the fixed time step $\Delta t = t_{j+1} - t_j$. Let us recall that the temporal derivative of solution at time $t = 0$ is computed using the initial conditions (17), while for any next $t = t_j$ we utilize representation (47).

We would like to underline here the fact that as the output of the proposed algorithm, one obtains not only the solution of the transient problem, that is, the crack length $L(t)$ and the crack opening $w(t, x)$, but also the temporal derivative of the latter, $w'_t(t, x)$ and the crack propagation speed, $V_0(t)$, from (20).

3.2 Solver based on a modified self-similar algorithm

Temporal derivative of the solution can be taken in the following form:

$$\frac{\partial W}{\partial t} = 2 \frac{W - w}{\Delta t} - \frac{\partial w}{\partial t}, \quad (56)$$

which gives the error of approximation of the order $O(\Delta t^2)$. Note that any other two-points finite difference definition yields only $O(\Delta t)$.

Unfortunately, a direct use of the algorithm formulated in section 2.1 is not, generally speaking, possible, as it may fail for small time steps. Indeed if one takes $\sigma = 2$ and sufficiently small value of Δt in the representation (49)₂, then the value of the parameter β may be far away from its optimal magnitude $\beta = 1/3$. This in turn, would at least result in a deterioration of the efficiency of computations.

On the other hand, it is quite clear that boundary value problem (26), (27) is solvable for large values of the parameter β . Indeed, performing asymptotic analysis, one shows that the solution can be represented in the form:

$$u(x) = -q_l^*(x) + b_0(x) + b_1(x), \quad x \in (0, 1), \quad (57)$$

where b_0 and b_1 refer to two boundary layers, accounting for the boundary conditions (27)₁ and (27)₂, respectively.

Thus the algorithm should be modified to be able to deal with large values of β . To achieve this goal, let us look at the original representation (34), where only the last term in the right-hand side depends on β . This term violates the convergence of the iterative process for large β . To prevent this from happening, at each iteration we supplement the term in question with an auxiliary so-called 'viscous' term in the form $\mathcal{V}(x) = \beta u_0^3(1-x)(C_0 + C_1(1-x))$, where the constants, C_0, C_1 , are computed by comparing both the original and the viscous terms. In this way one can construct a *modified* algorithm, schematically represented in the following manner

$$\begin{cases} G_3 \left(\beta^{(i)}, W_0^{(i+1)}, \Delta W^{(i)}, q_0^* \right) = 0, \\ \mathcal{V}^{(i+1)} = \mathcal{V}(W^{(i)}, \hat{q}_l^{*(i+1)}), \\ \Delta W^{(i+1)} = \hat{G}_{12} \left(\beta^{(i+1)}, W_0^{(i+1)}, \Delta W^{(i)}, \hat{q}_l^*, \mathcal{V}^{(i+1)} \right), \\ L^{(i+1)} = G_5 \left(W_0^{(i+1)} \right), \\ \frac{\partial W^{(i+1)}}{\partial t} = 2 \frac{W^{(i+1)} - w}{\Delta t} - \frac{\partial w}{\partial t}, \end{cases} \quad (58)$$

where

$$\begin{aligned} \hat{q}_l^* &= -w - \frac{\Delta t}{2} \left[\frac{\partial w}{\partial t} + q_l(t, x) \right], \\ \beta^{(i)} &= \frac{6}{\Delta t} \left(L^{(i)} \right)^2 \left(W_0^{(i)} \right)^{-3}. \end{aligned} \quad (59)$$

The function $q_0^*(t)$ is defined in the same way as previously (see (50)). At each time step the initial value of W is taken in the form (55). We do not show here the precise definition of the operator \hat{G}_{12} , as it may be easily derived by merging operators G_1 and G_2 with the viscous term $\mathcal{V}(x)$, where respective constants are computed, for example by the least squares method.

3.3 Analysis of the algorithms performance.

The aim of this subsection is to analyze and compare the performances of the algorithms formulated in subsections 3.1 and 3.2. To this end, the benchmark solution used previously for the self-similar formulation is utilized, for the time dependent term $\psi(t) = (1+t)^\gamma$ (compare (63)). First tests are performed for $\gamma = 1/5$.

In the following, the notations *solver 1* and *solver 2* are attributed to the algorithms (54) and (58), respectively.

Let us analyze the influence of the spatial mesh density on the accuracy of computations done by both solvers. For this reason, we start with a single time step (in our case $\Delta t = 10^{-2}$) and carry out the

computations for different numbers of nodal points N , ranging from 10 to 100. The following parameters are used for the comparison: the maximal relative error of the crack opening, δw , the relative error of the crack length, δL , and the maximal relative error of the temporal derivative of the crack opening, δw_t .

The results of computations are depicted in Fig. 4a). It shows that regardless of the considered parameter, *solver 2* always provides better accuracy (two orders of magnitude for the crack opening, w , and an order for the crack length, L). The only exception is for δw_t , whose values are of the same order and *solver 1* may even give a bit lower errors. However, this does not result in a better accuracy of the two remaining components of the solution: w and L . Note that for the first time step, the accuracy of computation of the crack length, $L(t)$, is of two orders of magnitude better than that for the crack opening, δw , regardless of the solver type and the number of the nodal points, N .

Similarly to the trend observed in the self-similar formulation, computational errors stabilize for some critical value $N = N_*(\Delta t)$. Surprisingly, for the transient regime where the temporal derivative plays a crucial role, the critical N_* appears to be even slightly lower than that for similarity solution. Thus, for both solvers it is sufficient to take only 40 points to achieve the maximal level of accuracy.

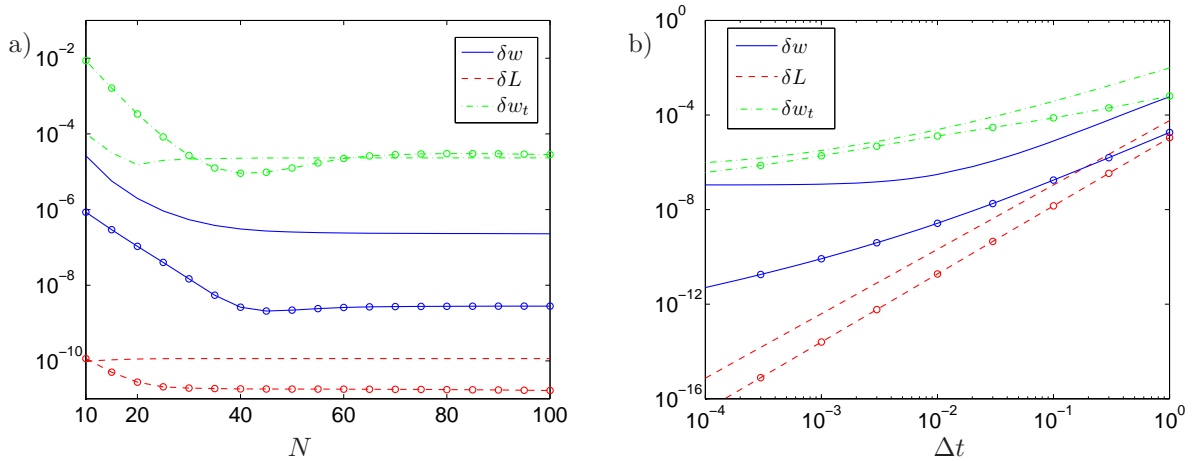


Figure 4: The errors of computations: $\delta L, \delta w, \delta w_t$ as functions of a) spatial mesh density (number of nodal points, N) for the fixed time step $\Delta t = 10^{-2}$; b) time step Δt for fixed number of the nodal points $N = 40$. Line with markers refer to *solver 2*

REMARK 2. From first glance it may be surprising that the accuracy of the temporal derivative, δw_t , is up to four orders of magnitude worse than that for δw in the case of *solver 2*. However, this fact can be easily explained when one analyses the estimation: $\delta w_t \approx 2w\delta w/(\Delta t w_t)$ which follows from (56) for small Δt . Computing the multiplier in the right hand side of the estimation, one obtains the respective value of the order of 10^4 . Note that the recalled formula does not account for the error of the method of w_t approximation itself. In some cases (very small time steps) this value may be comparable to the former, and thus essentially influence the overall error.

REMARK 3. At the first time step, there also exists a direct relationship between the error of the crack length, δL , and the multiplier of the leading term of the asymptotics (46), δW_0 . For small values of Δt it reads: $2\delta L = W_0^3 \delta W_0 \Delta t$. Having this relation we do not show a separate analysis for W_0 and consequently, V_0 .

All the results presented above were obtained for a single time step $\Delta t = 10^{-2}$. In order to illustrate the influence of Δt on the solution accuracy, a number of computations were done in the interval

$\Delta t \in [10^{-4}, 1]$ for a fixed number of nodal points, $N = 40$. The results describing the solution errors are shown in Fig. 4 b). One can conclude from them that the errors decrease when reducing the time step (at least in the analyzed range of parameters). Simultaneously, one can expect that this tendency should have its own limitation for a fixed number of the nodal points, N , and starting from some small value $\Delta t(N)$, it will reverse to the opposite. For both solvers, a fast decrease of δL is observed as Δt gets smaller ($\delta L \approx a10^{-4}\Delta t^3$ and $a \sim 1$).

Now let us analyze the accuracy of the solution on a given time interval $t \in [0, t_K]$. As, it follows from the results presented in [17] and [22], after the initial growth to the maximal value, the error of computations stabilizes at some level or even decreases, and thus further extending of the time interval does not contribute to the deterioration of accuracy. Bearing this in mind we take here $t_K = 100$. First we test how the number of time steps K affects the accuracy of computations within the same time stepping strategy. For both solvers we took a fixed number of spatial mesh points, $N = 40$, changing the number of time steps K from 10 to 300. The utilized time stepping strategy was the same as that used in [22] for the Crank-Nicolson scheme. It is given by the following equation ($i = 1, 2, \dots, K$):

$$t_i = (i-1)\delta t + \frac{t_K - (K-1)\delta t}{(K-1)^3}(i-1)^3, \quad (60)$$

where δt is a parameter controlling the first time step. Note that by increasing the value of K one distributes the time points near $t = 0$ almost uniformly.

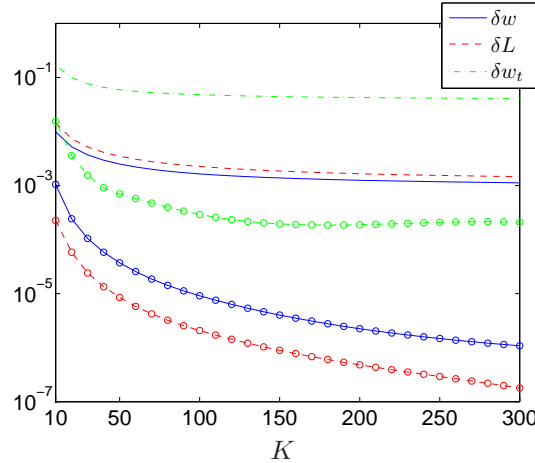


Figure 5: Influence of the number of time steps, K , within time stepping strategy (60), on accuracy of the computations for the fixed non-uniform spatial mesh ($N = 40, \varrho = 3$). Lines without markers correspond to *solver 1*, lines with markers refer to *solver 2*.

The achieved accuracy, as a function of the number of time steps K , is presented in Fig. 5. It shows that for the same value of K *solver 2* provides much more accurate results again and this advantage increases with growing K . One can expect, as it follows from the discussions after Fig. 4 which refers to a single time step, that each solver gives the solution errors satisfying the estimation: $\delta L \ll \delta w \ll \delta w_t$ for any set of the input parameters. Indeed, *solver 2* supports this statement as can be seen Fig. 5, while for *solver 1* surprisingly another trend is observed: $\delta w < \delta L < \delta w_t$.

To explain this apparent paradox, let us recall that all errors in Fig. 5 are taken as the maximal values over the time-space domain. However, since for the assumed time stepping strategy the time steps increase with growing time, one can expect (compare the results in the Fig. 4b)) that at some point δL may become greater than δw . Moreover, the error accumulation in successive time steps may

solver	N	K	δL	δw	δV_0	δw_t	$\delta w_t^{(FD_2)}$	$\delta w_t^{(FD_3)}$
from [22]	100	242	$6.8 \cdot 10^{-3}$	$5.0 \cdot 10^{-3}$	–	–	$4.1 \cdot 10^{-1}$ ($1.0 \cdot 10^{-2}$)	$4.1 \cdot 10^{-1}$ ($4.8 \cdot 10^{-3}$)
<i>solver 1</i>	40	30	$5.2 \cdot 10^{-3}$	$3.7 \cdot 10^{-3}$	$7.1 \cdot 10^{-3}$	$7.5 \cdot 10^{-2}$	$4.6 \cdot 10^{-2}$	$2.0 \cdot 10^{-2}$
<i>solver 2</i>	40	30	$2.4 \cdot 10^{-5}$	$1.1 \cdot 10^{-4}$	$3.2 \cdot 10^{-4}$	$1.5 \cdot 10^{-3}$	$4.6 \cdot 10^{-2}$	$3.4 \cdot 10^{-3}$
<i>solver 1</i>	5	30	$5.2 \cdot 10^{-3}$	$3.7 \cdot 10^{-3}$	$7.0 \cdot 10^{-3}$	$7.5 \cdot 10^{-2}$	$4.1 \cdot 10^{-2}$	$2.0 \cdot 10^{-2}$
<i>solver 2</i>	5	30	$8.0 \cdot 10^{-5}$	$5.7 \cdot 10^{-4}$	$6.3 \cdot 10^{-4}$	$5.6 \cdot 10^{-2}$	$6.3 \cdot 10^{-2}$	$6.2 \cdot 10^{-2}$

Table 1: Comparison of the results obtained for the solver developed in [22] and two integral solvers: *solver 1* and *solver 2*. The same benchmark solution with the leak-off vanishing near the crack tip is considered.

additionally influence the relationship between δL and δw , especially if they are close to each other as it is in the case of *solver 1*. Fig. 6 depicts the evolution of computational errors in time. For both solvers δw and δw_t reach their maximal values and stabilize or decrease for $t < t_K$. In the case of *solver 1* one can observe an intensive error accumulation for the crack length, δL . Indeed, it can be seen from the Fig. 6, that there exists a moment when the error curves for δL and δw intersect for the *solver 1*. In the case of *solver 2*, respective errors of solution (δL , δw and δw_t) have essentially different values. As a result, this effect does not take place in the time interval under consideration. However, it may be encountered for $t_K > 100$, as suggests the trend observed for t close to t_K .

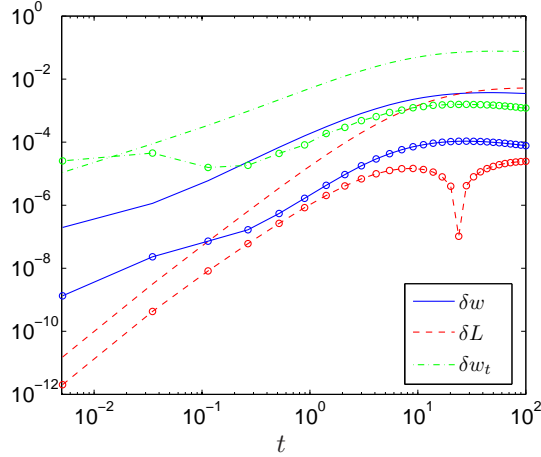


Figure 6: Distribution of the solution errors in time. Line with markers refer to *solver 2*. The time stepping strategy (60) is used for $K = 30$. The number of nodal points, $N = 40$.

It is interesting to compare the solution errors generated by the two integral solvers with those obtained in [22] for a dynamic system (DS) approach. In the latter case a standard MATLAB solver, *ode15s*, was employed. The best results were obtained for a uniform spatial mesh, the presented data corresponded to $N = 100$. The time stepping strategy chosen automatically by the solver (whose character is approximated by (60)) accepted 242 time steps. The maximal relative error of the crack opening, δw , and the crack length, δL , were $5.0 \cdot 10^{-3}$ and $6.8 \cdot 10^{-3}$ (see Table 1), respectively.

When analyzing the data collected in Table 1, one concludes that it is sufficient for any of the integral solvers to take only $N = 40$ nodal points and $K = 30$ time steps, as suggested the previous analysis, to have better (but comparable – *solver 1*), or much better (*solver 2*) results. Indeed, the

corresponding maximal errors for the integral solvers are: $\delta w = 3.7 \cdot 10^{-3}$, $\delta L = 5.2 \cdot 10^{-3}$ for *solver 1*, and $\delta w = 1.1 \cdot 10^{-4}$, $\delta L = 2.4 \cdot 10^{-5}$ for *solver 2*. In other words, the first solver provides the same accuracy for the crack opening and the crack length as the DS solver using much greater numbers of nodal points and time steps, while the second one, under the same conditions, improves the results at least one order of magnitude. It also shows that the *solver 2* yields one order of magnitude better accuracy of the crack propagation speed, V_0 , than the *solver 1*.

The new algorithms allow us to automatically compute the temporal derivatives in the solution process. The respective errors, δw_t , are: $7.5 \cdot 10^{-2}$ – *solver 1* and $1.5 \cdot 10^{-3}$ – *solver 2*. We decided to compare these figures, with the ones obtained in postprocessing (here, also the DS approach was examined). To this end two FD schemes (2-points and 3-points) were used. This time, the corresponding errors, δw_t , were: $4.6 \cdot 10^{-2}$ and $2.0 \cdot 10^{-2}$ for *solver 1*, $4.6 \cdot 10^{-2}$ and $3.4 \cdot 10^{-3}$ for *solver 2* and the same value $4.1 \cdot 10^{-1}$ for both schemes in the case of DS. It is worth mentioning that the values obtained for DS appeared at the first time step. Then, the errors decreased with time and stabilized to give their minimal levels of 10^{-2} and $4.8 \cdot 10^{-3}$, correspondingly.

As can be seen, the integral solvers give at least one order of magnitude better accuracy of w_t than the DS. Moreover, while the postprocessing gives smaller (but comparable) error for the *solver 1*, *solver 2* returns more accurate values of w_t than those obtained in the postprocessing, even for the 3-points FD. Finally, apart from the fact that δw and δL for the DS and *solver 1* look comparable in values, the quality of the computation is better for the new solver as is clear from the postprocessing analysis.

Just for comparison we also present in Table 1 the results obtained for the spatial mesh composed of only five nodal points, $N = 5$. It turned out that even for such a drastic reduction of the mesh density, the solution accuracy for most of the parameters is of the same order as for $N = 40$. Interestingly, *solver 1* exhibits almost no sensitivity to this mesh reduction. In fact the distinguishable differences can be observed only for the *solver 2*.

Let us now analyze the distribution of crack opening error, δw , in time and space. The respective results are presented in Fig. 7 a) – *solver 1*, and Fig. 7 b) – *solver 2*. In both cases the maximal errors are located at the crack tip while the error distribution in time follows the trend visible in Fig. 6.

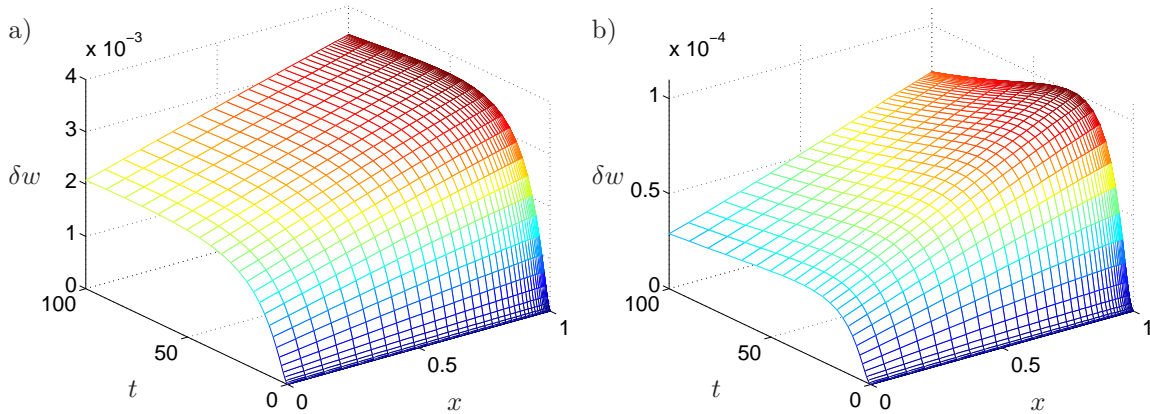


Figure 7: The relative error of the crack opening obtained for $N = 40$ (nonuniform mesh, $\varrho = 3$) and the time stepping strategy (60) with $K = 30$. Fig. 7a) corresponds to the *solver 1*, while Fig. 7b) refers to the *solver 2*.

Fig. 8 shows the distributions of δw_t obtained by the integral solvers. It confirms our previous observation, that *solver 2* always provides better results than *solver 1*. Moreover, the greatest error in

the case of *solver 1* is located at the crack inlet and the lowest at the crack tip, while *solver 2* gives approximately the same values of δw_t along the crack length.

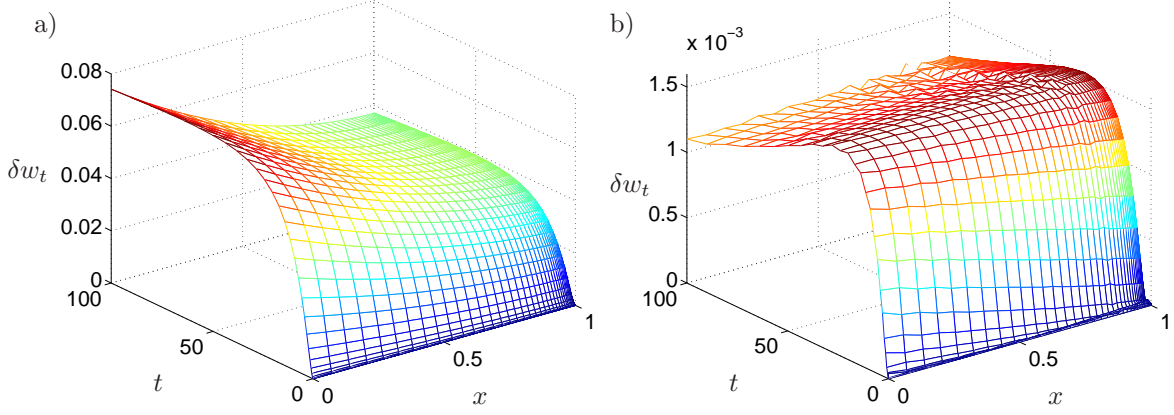


Figure 8: The relative error of the temporal derivative of the crack opening. Solution obtained by: a) *solver 1*, b) *solver 2* for $N = 40$, non-uniform mesh ($\varrho = 3$) and the time step strategy (60) with $K = 30$.

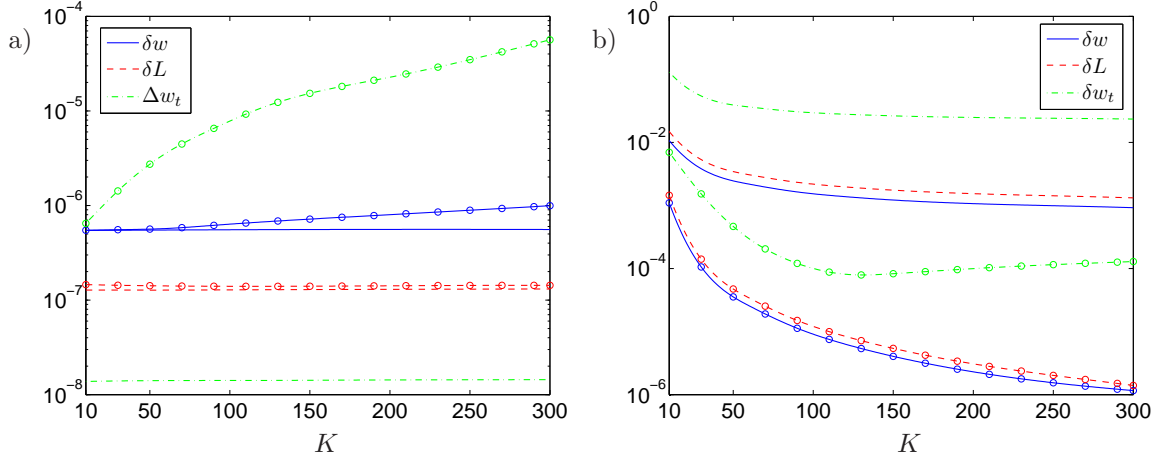


Figure 9: The errors of solution for two variants of γ : Fig. 9a) $\gamma = 0$, Fig. 9b) $\gamma = 1/3$. Line with markers correspond to *solver 2*.

In the last test in this subsection we analyze the relation between the regimes of crack propagation and the performances of respective solvers. As mentioned previously, the benchmark solution in form (29) can be used to imitate various dynamic modes of the crack evolution. So far we have utilized the exponent of the time dependent term of the value $\gamma = 1/5$ which refers to the constant injection flux rate. Now, let us consider two other variants of γ : i) $\gamma = 0$ - for this choice the normalized crack opening is constant in time; ii) $\gamma = 1/3$ - this value corresponds to the steady state propagation of the fracture. For the computations the same spatial mesh as before is taken ($N = 40$). The number of time steps accepted within strategy (60), K , ranges from 10 to 300. In this way the graphs (Fig. 9a)-b)) describing the solution errors in the function of K were prepared for both values of γ (similarly as in Fig. 5). The

analyzed accuracy parameters were: relative error of the crack opening, δw , relative error of crack the length, δL , relative error of the crack opening temporal derivative, δw_t , for $\gamma = 1/3$ and absolute error of the crack opening temporal derivative, Δw_t , for $\gamma = 0$.

The results depicted in Fig. 9 show that for $\gamma = 0$ one obtains much more accurate results than for $\gamma = 1/3$ that could have been predicted ($w_t = 0$). However, it is a surprise that for $\gamma = 0$ *solver 1* provides better solution accuracy than *solver 2*. Although the difference is moderate in case of δw and δL , the values of Δw_t vary by at least two orders of magnitude. From Fig. 9a) it follows that for this regime of crack propagation the solution accuracy cannot be improved by simple refining the temporal mesh, and for *solver 2* even a reverse relation is observed.

The situation is quite different for $\gamma = 1/3$ (Fig. 9b)). This time again *solver 2* proves its advantage over *solver 1* for all the analyzed parameters. For *solver 2*, it is sufficient to take only 30 time steps to have much better results than those provided by *solver 1* for 300 steps. The solution accuracy can be improved by increasing the number of time steps, however it seems that for *solver 1* the saturation level is close to $K = 300$. A similar trend was observed for $\gamma = 1/5$ (see Fig. 5).

A direct conclusion from this test is that for different modes of crack propagation there are different optimal time stepping strategies. This should properly accounted for especially in the cases when the values of injection flux rate or leak-off to formation change appreciably in the considered time interval.

The aforementioned analysis prove that in terms of accuracy in most of the cases *solver 2* is much better than *solver 1* with respect to all computed components of the solution: the crack length, L , the crack opening, w , its temporal derivative, w_t and the fracture propagation speed, V_0 . However, for some regimes of crack propagation (low values of γ) *solver 1* may give comparable or even slightly better results than *solver 2*. The advantage of *solver 1* is better efficiency of computations: the time of computations for this solver was on average one third lower than for *solver 2*.

3.3.1 Example with singular leak-off regime.

In (3) we have assumed that the behaviour of the leak-off function near the crack tip can be described by a power law, giving in the worst case a square root singularity. Such a limiting behaviour corresponds to the Carter leak-off model [5]. As a result, although the leading term of the asymptotic expansion for the crack opening near the fracture tip remains the same, the higher terms change, disturbing the solution smoothness (see [15]). A comprehensive analysis of this case was done in [17] where it was also proved that the deterioration of solution accuracy can be prevented by employing the second asymptotic term in the computational algorithm.

In this subsection we show that the algorithms developed in the paper are capable of tackling this kind of problems *without any additional modifications*. To this end let us consider another benchmark solution $u(t, x)$ (see (63)) defined by the functions:

$$h(x) = (1 - x)^{1/3}(1 + s(x)), \quad s(x) = \frac{1}{5}(1 - x)^{1/6}, \quad (61)$$

with the same function $\psi(t)$ with $\gamma = 1/5$.

One can easily check, that the above form of $s(x)$ results in a singular behaviour of q_l , with the leading term of the order $O((1 - x)^{-1/2})$ as $x \rightarrow 1$. The value of multiplier u_0 in (63) was taken in such a way to make the benchmark comparable with the one used previously, in a sense of an average particle velocity. Indeed, in [22] for a fluid velocity defined as $V = q/w$, a parameter describing its variation along the crack length was introduced:

$$\gamma_v(t) = \left[\max_x (V(x, t)) - \min_x (V(x, t)) \right] \left[\int_0^1 V(x, t) dx \right]^{-1}. \quad (62)$$

This parameter reflects indirectly the balance between the flux injection rate and leak-off to formation. It was also shown there that it has a decisive influence on the accuracy of computations (the greater

value of γ_v , the greater error of the computations). For the benchmarks with comparable values of γ_v , one can expect similar accuracy of the computations. This trend was also confirmed in [17]. In our case, the deterioration of the solution smoothness near the crack tip is an additional factor which contributes to the increase of the computational error.

Note that because of the chosen structure of (63), the value of γ_v is constant in time for all benchmarks considered in this paper. For the benchmark (43) γ_v yields 0.408, while (61) one leads to $\gamma_v = 0.411$.

The computations were done for the same spatial ($N = 40$, $\varrho = 3$) and temporal ($K = 30$, strategy (60)) meshes as previously considered. The distributions of the errors δw and δw_t are shown in Fig. 10 – Fig. 11, respectively. Comparing these results with those obtained for the finite leak-off regime (see Fig. 7 – Fig. 8) one can see that the accuracy of computations decreased significantly.

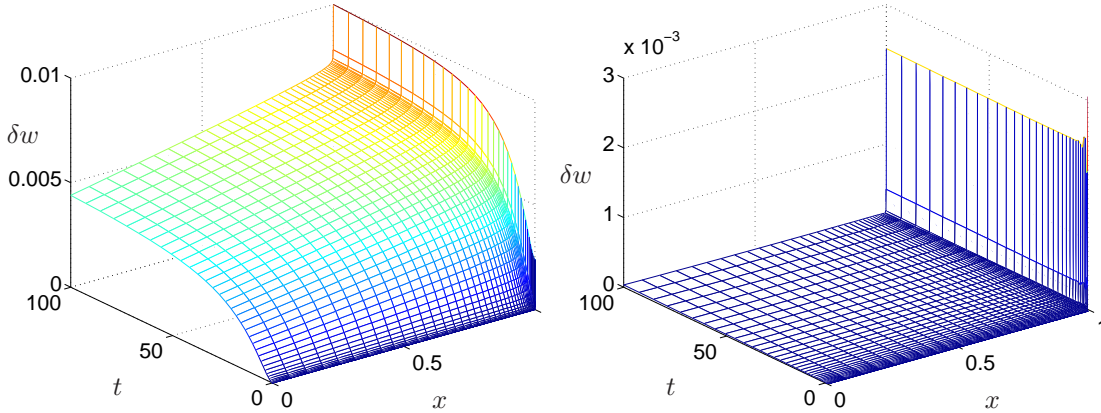


Figure 10: The relative error of the crack opening. Solution obtained by: a) *solver 1*, b) *solver 2*. Other parameters in the computations were: $N = 40$, $K = 30$, $\varrho = 3$.

In the case of *solver 1*, the crack opening error, δw , shown in Fig. 10 a) is of one order of magnitude greater than that reported in Fig. 7 a). For *solver 2* in turn, δw depicted in Fig. 10 b) is almost two orders higher than the one obtained previously for q_l vanishing at $x = 1$ (Fig. 7 b)). A pronounced jump of the error is observed at the crack tip, especially for *solver 2*, which explains the deterioration of accuracy when comparing with the finite leak-off case. However, if one considers the accuracy of the solution away from the crack tip, it is still of the same quality as before.

The same trend can be observed for the temporal derivative of the crack opening, w_t , see Fig. 11. Opposite to the benchmark case (43) with the finite leak-off, the distribution of δw_t for *solver 2* becomes highly non-uniform, with distinct increase at the crack tip.

This deterioration of the solution accuracy near $x = 1$ for the Carter leak-off model should not be a surprise, as the algorithm described above in (34) – (37) accounted directly only for the first (leading) term of the asymptotic expansion for the crack opening. For the singular leak-off model, the function Δu and other integrands employed in G_1 and G_2 are not sufficiently smooth near the crack tip, which increases the errors of integration. However, one can counteract this tendency by accounting for further asymptotic terms in the algorithm, which will be illustrated in the following with the example of two terms of w expansion.

Let us investigate the evolution of solution errors (δw , δL and δw_t) in time in the way it was done in Fig. 6 for the case of the finite leak-off. In Fig. 12 a) we show the results obtained by direct execution of the algorithm (34) – (37). Fig. 12 b) depicts the case of a modified algorithm employing also the second asymptotic term of the crack opening. When analyzing the results, one observes again the trend of δL

accumulation for both solvers. Interestingly, δL has the same level for both the original and the modified algorithms. In the case of *solver 1* for other analyzed parameters as well only a very slight improvement is reported. However, for *solver 2* one obtains a pronounced reduction of computational errors for w and w_t . To have a further advance here, the next terms of asymptotic expansion of the crack opening may be taken into account. On the other hand, for the Carter leak-off model the number of nodal points for which the accuracy saturation is observed is larger than for a finite leak-off. Thus, if necessary, one can also improve the accuracy by increasing the value of N and by taking a greater number of time steps K .

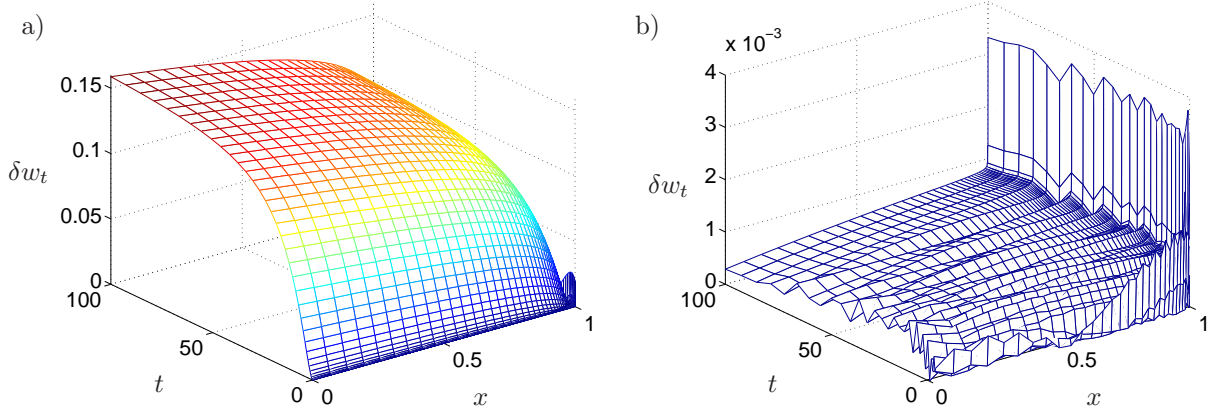


Figure 11: The relative error of the temporal derivative of crack opening. Solution obtained by: a) *solver 1*, b) *solver 2*. Other parameters in the computations are: $N = 40$, $K = 30$, $\varrho = 3$.

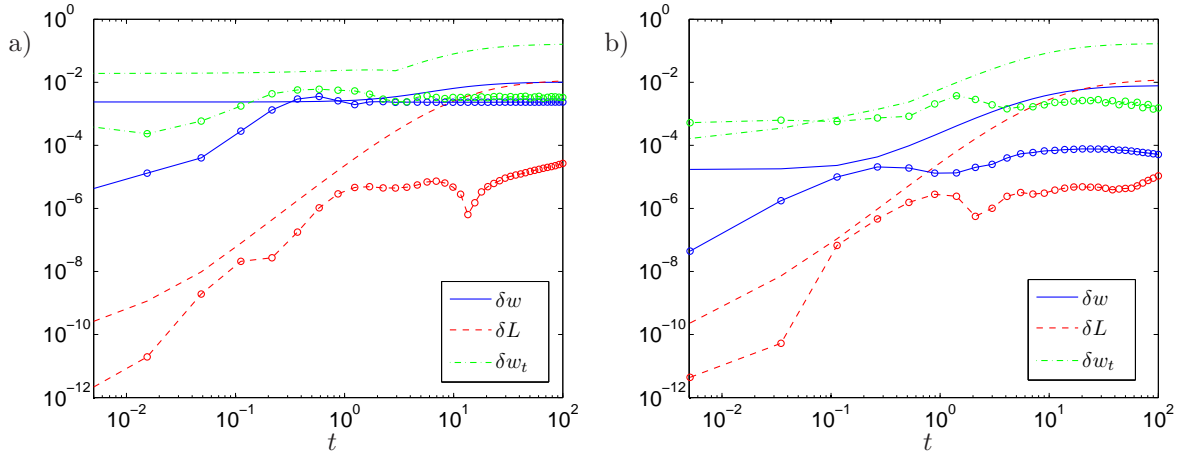


Figure 12: The relative error of the temporal derivative of crack opening. Solution obtained by: a) original algorithms, b) modified algorithms. The lines with markers refer to *solver 2*

From the analysis given in this subsection two main conclusions can be drawn. First, that the problems with singular leak-off regimes can be directly tackled by the proposed algorithms. Also in such cases *solver 2* yields more accurate results than *solver 1*. The second conclusion is that in order to

have the solution accuracy comparable to that achieved for non-singular leak-off, one has to use a larger number of nodal points and/or employ further terms of asymptotic expansion for w in the algorithm.

4 Conclusions

We would like to itemize the following conclusions as a resume of this paper:

- Presented approach can be efficiently used for tackling the PKN model of hydrofracturing and may be adopted for multifracture systems.
- Both new solvers provide better computational accuracy than the conventional algorithms from [22]. Moreover, comparable accuracies can be achieved here at much lower computational cost, as the new solvers enable us to drastically reduce the densities of spatial and temporal meshes.
- New solvers are appropriate for directly tackling the problems with different fluid flow regimes, including various injection flux rates and singular leak-off.
- In order to increase the efficiency and accuracy of computations, it is advisable to employ at least two asymptotic terms of the crack opening, w .
- The developed algorithms do not require any regularization techniques. The boundary conditions are imposed directly into the numerical scheme. The speed equation plays a crucial role in the analysis.

Acknowledgements

This work has been done in the framework of the EU FP7 PEOPLE project under contract number PIAP-GA-2009-251475-HYDROFRAC. The authors are grateful to the Institute of Mathematics and Physics of Aberystwyth University and EUROTCH Sp. z o. o. for the facilities and hospitality.

References

- [1] Adachi J, Detournay E (2002) Self-similar solution of a plane-strain fracture driven by a power-law fluid. *Int J Numer Anal Methods Geomech* 26: 579-604
- [2] Adachi J, Detournay E (2008) Plane strain propagation of a hydraulic fracture in a permeable rock. *Eng Fract Mech* 75(16): 4666-4694
- [3] Adachi J, Peirce A (2007) Asymptotic analysis of an elasticity equation for a finger-like hydraulic fracture. *J Elast* 90(1): 43-69
- [4] Adachi J, Siebrits E, Peirce A, Desroches J (2007) Computer simulation of hydraulic fractures. *Int J Rock Mech Min Sci* 44: 739-757
- [5] Carter E (1957) Optimum fluid characteristics for fracture extension. In: Howard, G., Fast, C. (eds.) *Drilling and Production Practices*, 261-270. American Petroleum Institute
- [6] Crittendon BC (1959) The mechanics of design and interpretation of hydraulic fracture treatments. *J Pet Tech* 21: 21-29
- [7] Detournay E (2004) Propagation regimes of fluid-driven fractures in impermeable rocks. *Int J Geom* 4: 1-11

- [8] Dobroskok AA, Linkov AM (2011) Modeling of fluid flow, stress state and seismicity induced in rock by instant pressure drop in a hydrofracture. *J Min Sci* 47(1): 10-19
- [9] Economides M, Nolte K (eds.) (2000) *Reservoir Stimulation*. 3rd edn. Wiley, Chichester, UK
- [10] Garagash DI, Detournay E (2000) The tip region of a fluid-driven fracture in an elastic medium. *J Appl Mech* 67: 183-192
- [11] Geertsma J, de Klerk F (1969) A rapid method of predicting width and extent of hydraulically induced fractures. *J Pet Tech* 21: 1571-1581 [SPE 2458]
- [12] Hubbert MK, Willis DG (1957) Mechanics of hydraulic fracturing. *J. Pet. Tech.* 9(6): 153-68
- [13] Kemp LF (1989) Study of Nordgren's equation of hydraulic fracturing. *SPE Production Eng* 5: 311-314
- [14] Khristianovic SA, Zheltov YP (1955) Formation of vertical fractures by means of highly viscous liquid. In: *Proceedings of the fourth world petroleum congress, Rome, 1955*, 579-586
- [15] Kovalyshen Y, Detournay E (2009) A reexamination of the classical PKN model of hydraulic fracture. *Transp Porous Med* 81: 317-339
- [16] Kovalyshen Y (2010) Fluid-driven fracture in poroelastic medium. PhD Thesis, The University of Minnesota
- [17] Kusmierczyk P, Mishuris G, Wrobel M (2012) Remarks on numerical simulation of the PKN model of hydrofracturing in proper variables. Various leak-off regimes. arXiv:1211.6474.
- [18] Lecampion B, Detournay E (2007) An implicit algorithm for the propagation of a hydraulic fracture with a fluid lag. *Comput Method Appl M* 196(49-52): 4863 – 4880
- [19] Linkov AM (2011) Speed equation and its application for solving ill-posed problems of hydraulic fracturing. *ISSM 1028-3358, Doklady Physics*, 56(8): 436-438. Pleiades Publishing, Ltd.
- [20] Linkov AM (2011) Use of a speed equation for numerical simulation of hydraulic fractures. arXiv:1108.6146
- [21] Linkov AM (2011) On efficient simulation of hydraulic fracturing in terms of particle velocity. *Int J Engng Sci* 52: 77-88
- [22] Mishuris G, Wrobel M, Linkov A (2012) On modeling hydraulic fracture in proper variables: stiffness, accuracy, sensitivity. *Int J Engng Sci* 61: 10-23
- [23] Mitchell SL, Kuske R, Peirce A (2007) An asymptotic framework for finite hydraulic fractures including leakoff. *SIAM J Appl Math* 67(2): 364–386
- [24] Mitchell SL, Kuske R, Peirce AP (2007) An asymptotic framework for the analysis of hydraulic fractures: the impermeable case. *ASME J Appl Mech* 74(2): 365–372
- [25] Moos D (2012) The importance of stress and fractures in hydrofracturing and stimulation performance: a geomechanics overview. *Search and Discovery Article* 80255 (2012)
- [26] Nordgren, RP (1972) Propagation of a Vertical Hydraulic Fracture. *J Pet Tech* 253: 306-314
- [27] Olson JE (2008) Multi-fracture propagation modeling: Applications to hydraulic fracturing in shales and tight gas sands. The 42nd U.S. Rock Mechanics Symposium (USRMS), June 29 - July 2, 2008, San Francisco, CA

- [28] Peirce A, Detournay E (2008). An implicit level set method for modeling hydraulically driven fractures. *Comput Methods Appl Mech Engrg* 197: 2858–2885
- [29] Peirce A, Detournay E (2009), An eulerian moving front algorithm with weak-form tip asymptotics for modeling hydraulically driven fractures. *Num Meth Eng* 25(2): 185-200
- [30] Perkins TK, Kern LR (1961) Widths of hydraulic fractures. *J Pet Tech* 13(9): 37-49 [SPE 89]
- [31] Rubin AM (1995) Propagation of magma filled cracks. *Ann Rev Earth Planet Sci* 23: 287-336
- [32] Sneddon IN, Elliot HA (1946) The opening of a Griffith crack under internal pressure. *Q Appl Math* 4: 262-267
- [33] Stoer J, Bulirsh R (2002) *Introduction to Numerical Analysis*. Third Edition. Springer-Verlag.
- [34] Tsai VC, Rice JR (2010) A model for turbulent hydraulic fracture and application to crack propagation at glacier beds. *J Geophys Res* 115: 1-18
- [35] Zhang X, Jeffrey R, Llanos EM (2004) A study of shear hydraulic fracture propagation. Gulf Rocks 2004, the 6th North America Rock Mechanics Symposium (NARMS), June 5 - 9, 2004 , Houston, Texas

Appendix A: Numerical benchmarks

Let us define a set of benchmark solutions useful for testing different numerical solvers. Consider a class of positive functions $C_+(0, 1)$ described in the following manner:

$$C_+(0, 1) = \{h \in C^2(0, 1) \cap C[0, 1],$$

$$\lim_{x \rightarrow 1-} (1-x)^{-1/3} h(x) = 1, \quad h(x) > 0, \quad x \in [0, 1)\}.$$

By taking an arbitrary $h \in C_+(0, 1)$, one can build a benchmark solution for the normalized formulation of the problem as:

$$u(x) = u_0 \psi_j(t) h(x). \quad (63)$$

where functions $\psi_j(t)$ and $h(x)$ are specified below. On substitution of (63) into (26) one finds:

$$q_l(t, x) =$$

$$\gamma u_0 \left[\frac{1}{\beta} \left(x h^3(x) h'(x) + 3 (h^3(x) h'(x))' \right) - h(x) \right] \psi_j^\alpha(t),$$

$$w_0(t) = u_0 \psi_j(t),$$

where two sets of the benchmark solutions can be considered. For the first one we choose $\psi_1(t) = e^{\gamma t}$ and $\beta = 2/3$, $\alpha = 1$, while for the second, $\psi_2(t) = (a + t)^\gamma$ and $\beta = 2\gamma/(3\gamma + 1)$, $\alpha = (3\gamma - 1)/\gamma$. Corresponding crack lengths are defined in (25) and (30), respectively. Finally, the injection flux rate is computed from the boundary condition (16)₁:

$$q_0(t) = -\frac{u_0^4 \psi_j^4(t)}{L(t)} h^3(0) h'(0), \quad (65)$$

while the initial condition reads $W(x) = u_0 \psi_j(0) h(x)$.

Note that when taking the function $h(x)$ from the class $C_+(0, 1)$ in the following representation:

$$h(x) = (1 - x)^{1/3}(1 + s(x)),$$

$$s \in C^2[0, 1], \quad s(x) > -1, \quad x \in [0, 1)$$

q_l automatically satisfies the condition $q_l(t, x) = O((1 - x)^{1/3})$, $x \rightarrow 1$.

The presented benchmarks allow one to test numerical schemes in various fracture propagation regimes (accelerating/decelerating cracks) by choosing proper values of the parameter γ (see [22]). Additionally, if one reduces the requirements for the smoothness of $s(x)$ near $x = 1$, assuming that $h \in C^2[0, 1) \cap H^\alpha(0, 1)$ the benchmark can serve to model singular leak-off regimes (compare with (61)).

Note that the zero leak-off case cannot be described by the aforementioned group of benchmarks. However, an analytical benchmark for this regime, represented in terms of a rapidly converging series, has been developed in [21].